https://doi.org/10.2352/CIC.2022.30.1.36

Image quality of spectral filter arrays for planetary rover applications: from demosaicing to color correction

E. Cucchetti[a], *E. Robert*[a,b,c], *A. Delahaye*[d], *M. Boutillier*[a], *C. Latry*[a], *K. Mathieu*[a], *N. Théret*[a], *C. Virmontois*[a]

[a] *Centre National d'Etudes Spatiales, 18 Av. Edouard Belin Toulouse, France*
[b] *ISAE Supaero, 10 Av. Edouard Belin Toulouse, France*
[c] *Munsell Color Science Laboratory, Rochester Institute of Technology, 54 Lomb Memorial Dr, Rochester, NY, USA*
[d] *Magellium, 1 Rue Ariane, 31520 Ramonville-Saint-Agne, France*

Abstract

The exploration of the Solar System using unmanned probes and rovers has improved the understanding of our planetary neighbors. Despite a large variety of instruments, optical and near-infrared cameras remain critical for these missions to understand the planet's surrounding, its geology but also to communicate easily with the general public. However, missions on planetary bodies must satisfy strong constraints in terms of robustness, data size and amount of onboard computing power. Although this trend is evolving, commercial image-processing software cannot be integrated. Still, as the optical and a spectral information of the planetary surfaces is a key science objective, spectral filter arrays (SFAs) provide an elegant, compact and cost-efficient solution for rovers. In this contribution, we provide ways to process multi-spectral images on the ground to obtain the best image quality, while remaining as generic as possible. This study is performed on a prototype SFA. Demosaicing algorithms and ways to correct the spectral and color information on these images are also detailed. An application of these methods on a custom-built SFA is shown, demonstrating that this technology represents a promising solution for rovers.

Introduction

The use of CCD and CMOS arrays coupled with deposition techniques of selective wavelength filters has become a cost-efficient way to produce optical color cameras, with the creation of color filter arrays (CFAs) [1, 2], followed by spectral filter arrays (SFAs) [3]. These detectors provide a sparse representation of multiple spectral bands from the optical to the near infrared (NIR) on a single detector, compacting the information on a unique pixelated image. The extension of these cameras to remote sensing applications shortly followed, with various missions being equipped with CFAs. Notable examples include the Remote Micro-Imager on board of the *Perseverance* rover on Mars [4], or the future navigation cameras of the *Mars Moon eXplorer* (MMX) rover [5]. More recently, SFAs started being considered as complementary to CFAs for Earth observation missions, e.g., WorldView3 (WV3) [6] satellites. In such cases however, SFAs are organized as lines and exploit the orbital movement of the satellite to acquire spectral bands through push-broom techniques. The French Space Agency (CNES), is considering the use of pixelated SFAs for planetary missions and rovers.

In this paper, we analyze the main aspects of the image quality (IQ) of SFA cameras for planetary applications. A prototype camera provided by SILIOS covering the 580 nm-1000 nm range with eight spectral bands is used as a test case. The selected spectral bands are *not* optimized for color detection, but rather for planetary science investigation. Further, due to the fabrication process of the spectral filters the wavelength choice cannot accommodate both NIR and blue bands [7]. A first challenge is to provide full-resolution images through demosaicing (see [8]). After reviewing techniques satisfying our constraints, we selected a non-local demosaicing providing satisfactory results. Filter deposition techniques cause however non-negligible spectral rejection between bands, which needs to be corrected to increase spectral accuracy. This aspect is investigated and corrected in the second part of this paper, starting from quantum efficiency (QE) measurements taken at CNES. Finally, once radiometric corrections are performed, ways of visualizing and exploiting multi-spectral images are discussed. Even though a perceptual colorimetric correction is not possible due to the lack of the blue optical spectrum in our SFA, tentative techniques to recover equivalent sRGB images are analyzed, inspired from [9]. This is performed by applying a color-correction matrix (CCM) [10, 11] estimated through calibration of the camera with/without IR cut-off filters. This work is a preliminary effort to optimize the SFA configuration to obtain faithful spectral, spatial and colorimetric results in future cameras.

Custom SFA matrix and data set

Optical and NIR cameras are essential for planetary science, but provide a limited view of the geology and the reflectances of rocky planetary surfaces. Spectroscopic instruments can compensate for this lack, losing however the spatial resolution provided by the cameras [12]. In this regard, SFAs offer a compromise between spatial and spectral resolution. As a preliminary analysis of SFAs for future rover missions, we have used a custom-build SFA provided by SILIOS, based on an AMS CMV4000 mounted on a 3D PLUS cube [13]. This development, detailed in [7], assessed the feasibility of spectral filter deposit on flight-hardware. Final choices on band configurations, pixel shape and spectral band selection remain open to date. The camera is divided into two sections of 2048×1024 pixels (see Figure 1). The left side of the matrix has usual square filters, whereas the right side has octagonal filters. The latter were deposited as a test to improve signal-to-noise ratio in spectral bands [7], but were not considered in this study as results in IQ/rejection were found to be equivalent. The SFA is composed of a 4×4-pixel pattern including 8 spectral bands (see Table 1) and 8 panchromatic bands in quincunx. Panchromatic bands were purposely maintained in the design to obtain reference images for demosaicing and to ensure an alias-free band for detailed texture observation. To obtain a working data set of multi-spectral images, we performed acquisition on a

Figure 1. *(**Left**) Pixelated pattern of custom SFA, bands are provided in Table 1. (**Right**) Examples of raw images acquired by the custom SFA. Vignetting is due to the optical system used for data acquisition (aperture $\approx f/4$) and is corrected during image processing (through a flat-field) after dark signal subtraction. A variety of scenes were used to account for specular reflections, granularity, textures and wide dynamic-range.*

variety of scenes, shown in Figure 1. These include sharp structures (edges) to test aliasing features, as well as multi-color features for rejection investigations. Images used in this paper are systematically corrected of dark signal and flat-fielded. This data is completed by WV3 satellite acquisitions, which possess also eight spectral bands from 400 to 1040 nm at full resolution [6], used as reference to test our corrections (e.g., demosaicing).

Demosaicing of multi-spectral images

SFAs condense N spectral bands on a single image. This is highly beneficial as telemetry and image compression are critical in rover applications. The main complexity of recovering full-resolution images lies in the demosaicing [3].

Theory: demosaicing approach

For space applications, we distinguish three main types of demosaicing techniques: 1) the use of super-resolution algorithms [14], 2) the use of blind or convolutional neural networks (CNNs) techniques which start from a reference data set to provide the best estimate demosaiced image [15], or 3) the use of interpolation techniques (spatial and/or spectral) which only use the information of a single image [8]. For rovers, the first option is difficult to implement, as the number of images and/or the computing power on board must remain small. CNN-based techniques offer an interesting solution, however the training data set is complex to obtain, as Earth-based images are used to describe other bodies of the Solar System. In our case, a more 'classic' approach based on interpolation was studied. In this regard, number of straightforward techniques exist but are faced with problems of aliasing. Minimization techniques assuming a known radiance [16] represent a very promising option for future investigations, but require reference data bases and the knowledge of the planetary illuminant which remain to be determined, but are actively investigated e.g. for Martian applications [11, 12]. As planetary images are often strongly affected by acquisition conditions (noise) and compression, coupling demosaicing and denoising becomes an interesting option. Non-local (NL) methods were thus retained as interesting candidates for demosaicing [17].

Method: custom NL demosaicing

Non-local (NL) methods imply the auto-similarity of the scene, i.e. that similar features are observed in different parts of the field-of-view. This assumption is particularly true for Earth observation, and should be well verified for planetary surfaces with rocky landscapes, typical of small bodies of the Solar System. The advantage of NL methods is their capability of denoising and demosaicing simultaneously, which is beneficial for rover images, where shot noise is often important.

Band	Centroid λ_0 (nm)	Width $\Delta\lambda$ (nm)
Panchromatic	790	210
Band 1	580	40
Band 2	640	40
Band 3	700	40
Band 4	760	40
Band 5	820	40
Band 6	860	40
Band 7	920	40
Band 8	980	40

Table 1: Spectral bands of custom SFA

For our pattern, the panchromatic band is finely sampled within a coarsely sampled grid of spectral pixels. This design is motivated by the will to preserve panchromatic images onboard future rovers. Our demosaicing starts from the panchromatic band through a gradient-based interpolation [18]:

1) For a missing panchromatic pixel p at location i,j of a spectral band b, vertical ΔV and horizontal gradients ΔH are computed[1]: $\Delta H = |p_{i+1,j} - p_{i-1,j}| + |2b_{i,j} - b_{i+4,j} - b_{i-4,j}|$, $\Delta V = |p_{i,j+1} - p_{i,j-1}| + |2b_{i,j} - b_{i,j+4} - b_{i,j-4}|$.The missing pixel $p_{i,j}$ is interpolated depending on the gradient:

- $\hat{p}_{i,j} = 0.5(p_{i,j-1} + p_{i,j+1}) + 0.25(2b_{i,j} - b_{i,j+4} - b_{i,j-4})$, if $\Delta H > 1.5\Delta V$
- $\hat{p}_{i,j} = 0.5(p_{i-1,j} + p_{i+1,j}) + 0.25(2b_{i,j} - b_{i+4,j} - b_{i-4,j})$, if $\Delta V > 1.5\Delta H$,
- else, $\hat{p}_{i,j} = 0.25(p_{i,j-1} + p_{i,j+1} + p_{i-1,j} + p_{i+1,j})$

2) Spectral bands are assumed to have the same high frequencies as the panchromatic band[2]. Under this 'constant-hue' assumption, we compute a hue band $H_i = B_i - \beta_P \hat{P}$ by subtracting the estimated panchromatic image $\hat{P}$ (with a weighting parameter β_P)

[1] Diagonal next-neighbor gradients can also be added, but do not improve results, while significantly improving computing time.

[2] Spectral bands are also strongly affected by the panchromatic bands due to fabrication, strengthening this assumption, see Figure 3

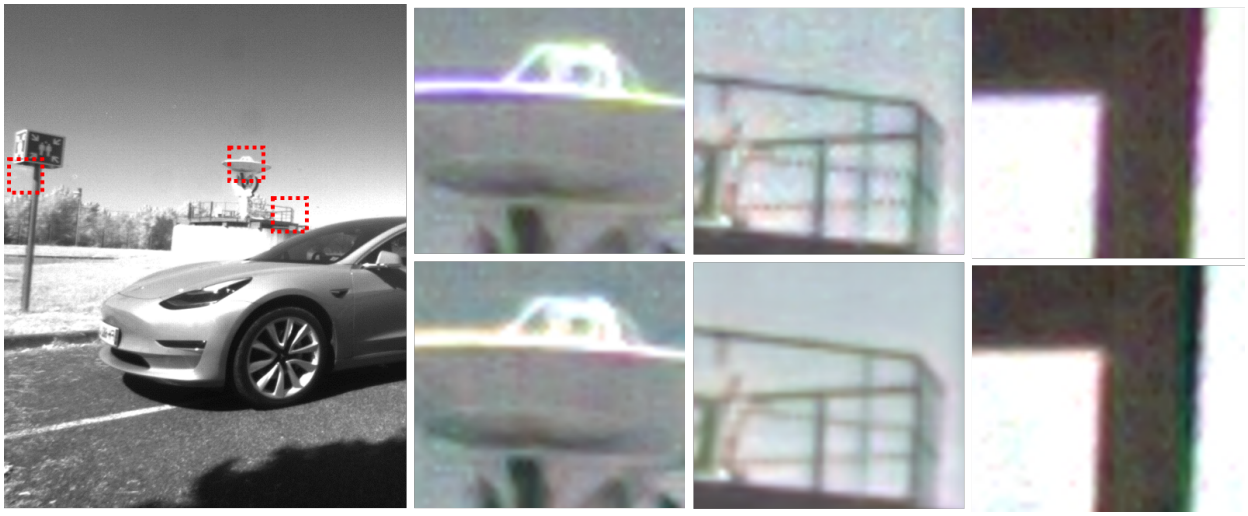

Figure 2. *(**Left**) Example of panchromatic image obtained after demosaicing and denoising for square filters. Within this image, three areas are zoomed (red dashed squares). (**Right**) Zoomed areas in false colors (B4/B2/B1) to illustrate image quality defects of the first demosaicing (**Top row**) and subsequent improvements (**Bottom row**). The dynamic range of the righter-most panel is modified to enhance zipper effects. The use of adjacent bands and joint denoising strongly reduces iridescence and zipper effects (particularly on railing in central zoom panel).*

to the band B_i. H_i is interpolated through bilinear interpolation to obtain $\hat{H}_i$. The band estimate is then $\hat{B}_i = \hat{H}_i + \beta_P \hat{P}$.

3) Finally, all bands go independently through a NL Bayes denoising [17]. To ensure that noise models are properly propagated through denoising, a variance stabilizing transform (e.g. an Anscombe transform) is performed before denoising and inverted afterwards. NL denoising is based on a similarity criteria between groups of $k \times k$ pixels (e.g., 5×5) called 'patches'. Patches are considered similar if their $\mathscr{L}^2$-norm is below a given threshold, taken as the local noise level standard deviation here.

Results and optimizations

As shown Figure 2, this demosaicing provides satisfactory results, although zipper artifacts and iridescence remain visible on pixel scales. These artifacts are particularly striking when spectral bands are visualized in false colors, by creating pseudo three-channel images. Several improvements were therefore put forward to improve the overall image quality.

Adjacent bands correlation – Zipper artifacts are related to the undersampling of the spectral bands. However, if we assume that adjacent bands have similar high-frequency features, likely to create zipper/iridescence artifacts, their correlated information can be leveraged to improve image quality. Instead of computing H_i directly, we determined the local average $B'_i = B_i - \bar{B_{i,j}}$, where $\bar{B_{i,j}}$ is the average of nearby pixels in adjacent bands of B_i[3]. We then compute $H'_i = B'_i - \beta_P \hat{P}$ and interpolate it as in the previous section to obtain $\hat{H}'_i$. The final band is obtained by averaging $\hat{H}^w_i = \hat{H}'_i \gamma + (1-\gamma)\hat{H}_i$, before adding $\beta_P \hat{P}$.

As both β_P and γ are free parameters, they offer degrees of freedom to optimize our demosaicing. However, as no multispectral data set representative of our SFA's spectral range was found, WV3 data of Earth providing eight spectral bands and a panchromatic band at full resolution was used instead. This constitutes a controlled data set to estimate the quality of our demosaicing through root-mean squared error (RMSE) metrics and visual inspection. Multiple β_P and γ combinations were tested (see Table 2). Comparison is performed between undersampled and subsequently demosaiced WV3 images I, and original images I_0. For a more meaningful comparison, a normalized RMSE using the noise standard deviation σ is introduced

$$RMSE_n(I, I_0) = RMSE(I/\sigma, I_0/\sigma)$$

When $RMSE_n$ is lower than 1, the demosaicing error is smaller than the noise level. As expected, γ has a stronger influence than β_P, as it represents a 'mixing' factor between bands. Its value affects the presence of Moiré effects and iridescence in the final WV3 images. An optimum is found for $\beta_P = 0.8$, $\gamma = 0.25$.

These values are subsequently propagated to SFA data, assuming the same conclusion hold, as no full-resolution data set is available in this case. Visually, these provide a satisfactory IQ (see example Figure 2), although there is no insurance that these values are optimal. This improvement visibly reduces zipper effects (Figure 2, bottom zoom panels).

$\gamma \setminus \beta_P$	0.5	0.6	0.7	***0.8***	0.9
0.05	0.901	0.900	0.899	0.899	0.899
0.15	0.891	0.888	0.887	0.885	0.884
0.25	0.885	0.882	0.880	***0.870***	0.875
0.50	0.898	0.893	0.891	0.892	0.896
0.75	0.942	0.937	0.939	0.947	0.960

Table 2: Normalized RMSE between demosaiced and reference image for different β_P and γ.

Joint denoising – Another improvement was included in the NL denoising by considering each band jointly during denoising, through a $\mathscr{L}^2$-norm similarity criterion on concatenated spectral

[3] Either the next spectral band, or the two adjacent bands

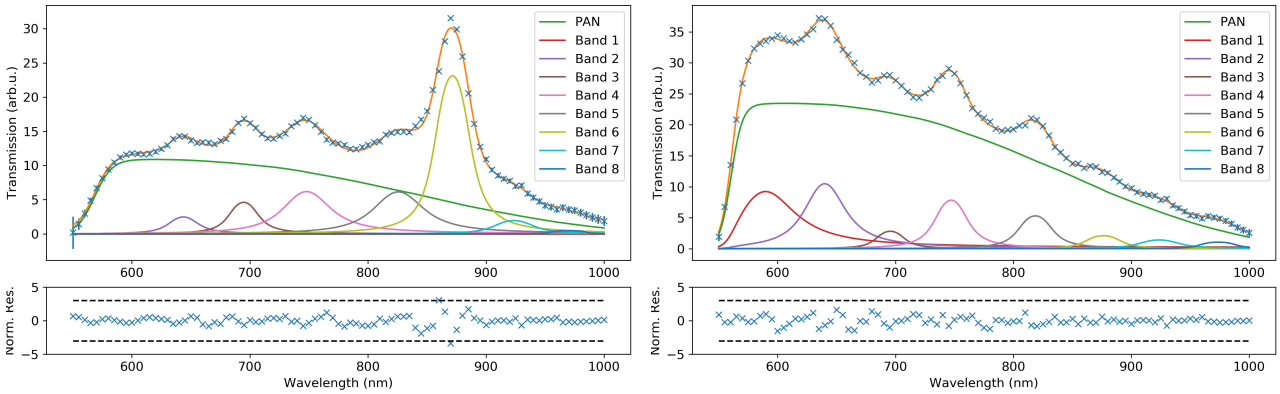

Figure 3. *Effective QE measured at CNES (blue 'x') for B6 (***Left***) and P6 (***Right***) bands defined Figure 1 (*Left*). The orange line is the best fit. Residuals (in standard deviation) are also shown. Individual channel contributions overlaid and are used to compute rejection between bands.*

patches. This refinement provides a visible reduction of iridescence artifacts (see Figure 2, central zoom panels).

These optimizations provide a satisfactory IQ, sufficient for early characterizations of SFAs. We notice however that the demosaicing (and spectral rejection correction, see below) tends to reduce the contrast of images, due to averaging and interpolation effects. Preliminary results show that contrast can be recovered through deconvolution and is not deemed critical in this case. On the contrary, though our NL approach maintains the local average of images, it can modify – sometimes significantly – the raw value of the pixel. Early tests of linear illuminant-based demosaicing [16] are ongoing, and will be tested on real acquisitions other planetary bodies (e.g. Moon). Both improvements will be investigated in a forthcoming work, also as ways to obtain more reliable information on the radiances of the observed scenes.

Spectral rejection correction

The overlapping spectral responses of the SFA's bands degrade the final spectral accuracy. We investigate in this section ways to model this pollution and means to correct it.

QE models for SFAs

The fabrication process of SFAs has a direct impact on the spectral response of the detectors [7]. Our detector is fabricated by depositing Fabry-Perot (FP) thin filters and a low-wavelength cut-off filter (below 550nm) on top of the micro-lenses of the original CMV4000 panchromatic camera. Measurements of the QE are possible through flat-field monochromatic light, but provide in fact an 'effective' QE including the filters' transmission. Dedicated measurements were performed at CNES and at ISAE (see Figure 3 for the square filters, results differ slightly for octagonal filters, not shown here). The effective QE is a linear composition of the panchromatic detector's QE (made of a Si substrate) and the FP transmission. The former is:

$$PAN(\lambda) = A \times (1 - R_{Si}(\lambda))(1 - exp(\varepsilon_{Si}(\lambda)e))$$

where A is the amplitude, R and ε respectively the reflectivity (unitless) and the absorption coefficient (in m^{-1}) of Si [19], while e is the thickness of the substrate (a few mm, measured). In turn, the individual FP transmission is given by

$$B_i(\lambda) = \frac{K_i}{(1 + C_i^2(\sin(\frac{\Lambda_i \cos(\theta)}{\lambda}))}$$

where K_i is the unitless amplitude, $C_i = 2\sqrt{R_i}/(1-R_i)$ with R_i the reflectivity, and $\Lambda_i = 2\pi n e_i$ with n the refraction index and e_i the FP thickness. The previous expression is provided for one incidence angle θ. Assuming a given aperture of the optics, with a maximum angle of incidence θ_M of the medium, the average transmission can be derived by integrating over θ to obtain:

$$B_i(\lambda) = K_i(f(C_i, \Lambda_i/\lambda, \theta_M) - f(C_i, \Lambda_i/\lambda, 0))$$

where

$$f(C_i, L_i, \theta) = -\frac{\arctan\left(\sqrt{C_i^2+1}\ \tan(L_i\ \cos(\theta))\right)}{\sqrt{C_i^2+1}\ L_i\ (1-\cos(\theta_M))}$$

QE measurements were fitted independently by assuming that $QE(\lambda) = F(\lambda)(PAN(\lambda) + \Sigma_i B_i(\lambda))$, where F is the measured filter transmission [7]. Amplitudes, centroids and values of Λ_i, C_i, e were left as free parameters. An example of QE model is provided Figure 3 for an optical aperture of $N = 4$.

QE-based correction

As shown in Figure 3, spectral bands are significantly polluted by neighboring bands, causing signal leaks which can hinder the interpretation of images. Interestingly, not only spatially-adjacent bands, but also distant bands contribute to the effective QE (see B_7 contribution in B_6). This effect is not properly understood, and is being characterized through dedicated measurements. A possible explanation may be related to the angle of incidence ($\approx 10/15°$) and the thickness of the FP, causing incident photons to be back-scattered up to several pixels in distance.

Assuming that the spectral contamination is isotropic, we can model it as an inverse problem $Y = AX$. Y is the observed (demosaiced) image, X the 'true' image before spectral contamination, and A a rejection matrix, where $a_{n,m}$ is the fraction of signal from band n in band m (see Figure 3). For panchromatic

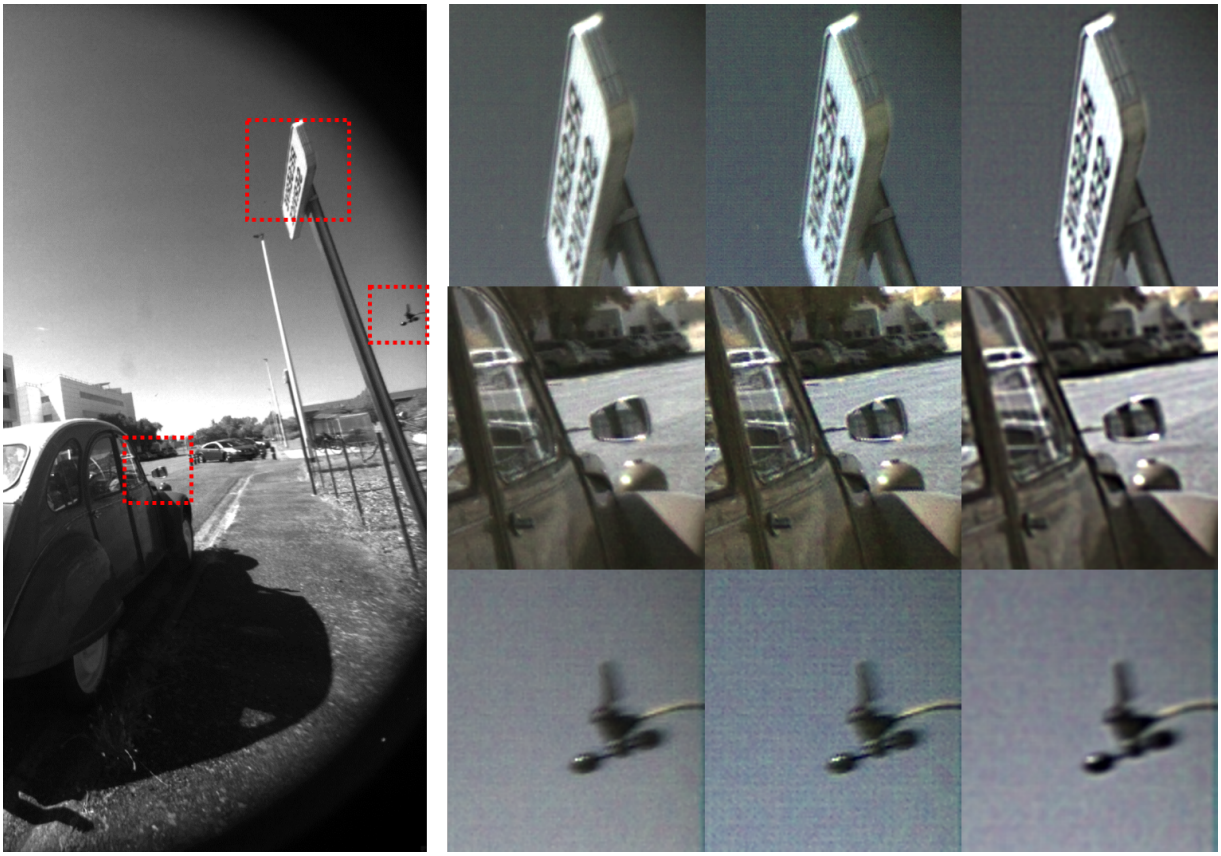

Figure 4. *(**Left**) Example of panchromatic image obtained after demosaicing and denoising for octogonal filters. Within this image, three areas are zoomed (red dashed squares). (**Right**) Zoomed areas in false colors (B4/B2/B1) to illustrate spectral rejection corrections. (**From left to right**) No correction, multiplicative spectral rejection, blind correction.*

	P1	P2	P3	P4	P5	P6	P7	P8	B1	B2	B3	B4	B5	B6	B7	B8
P1	0.70	0.00	0.00	0.00	0.00	0.00	0.00	0.00	0.08	0.04	0.03	0.04	0.03	0.05	0.02	0.00
P2	0.00	0.69	0.00	0.00	0.00	0.00	0.00	0.00	0.09	0.06	0.04	0.04	0.05	0.02	0.01	0.00
P3	0.00	0.00	0.70	0.00	0.00	0.00	0.00	0.00	0.06	0.04	0.01	0.08	0.06	0.03	0.02	0.00
P4	0.00	0.00	0.00	0.71	0.00	0.00	0.00	0.00	0.06	0.08	0.03	0.04	0.05	0.03	0.02	0.00
P5	0.00	0.00	0.00	0.00	0.67	0.00	0.00	0.00	0.05	0.07	0.01	0.08	0.04	0.05	0.02	0.00
P6	0.00	0.00	0.00	0.00	0.00	0.65	0.00	0.00	0.07	0.09	0.01	0.07	0.05	0.03	0.01	0.00
P7	0.00	0.00	0.00	0.00	0.00	0.00	0.67	0.00	0.09	0.05	0.01	0.07	0.05	0.05	0.01	0.00
P8	0.00	0.00	0.00	0.00	0.00	0.00	0.00	0.69	0.07	0.09	0.04	0.04	0.03	0.04	0.01	0.00
B1	0.06	0.06	0.06	0.00	0.00	0.00	0.06	0.00	0.53	0.00	0.01	0.07	0.07	0.05	0.02	0.00
B2	0.00	0.00	0.00	0.06	0.06	0.06	0.00	0.06	0.05	0.53	0.01	0.05	0.07	0.04	0.02	0.00
B3	0.06	0.06	0.00	0.06	0.00	0.00	0.00	0.06	0.00	0.13	0.44	0.03	0.08	0.05	0.02	0.00
B4	0.00	0.00	0.07	0.00	0.07	0.07	0.07	0.00	0.02	0.03	0.13	0.42	0.03	0.06	0.02	0.00
B5	0.00	0.11	0.00	0.00	0.00	0.11	0.11	0.11	0.00	0.03	0.04	0.11	0.34	0.02	0.02	0.00
B6	0.12	0.00	0.00	0.00	0.12	0.00	0.12	0.12	0.00	0.03	0.04	0.10	0.09	0.24	0.01	0.01
B7	0.00	0.12	0.12	0.12	0.00	0.12	0.00	0.00	0.00	0.04	0.05	0.11	0.10	0.09	0.12	0.00
B8	0.12	0.00	0.12	0.12	0.12	0.00	0.00	0.00	0.01	0.06	0.05	0.12	0.12	0.07	0.03	0.05

	P1	P2	P3	P4	P5	P6	P7	P8	B1	B2	B3	B4	B5	B6	B7	B8
P1	0.57	0.06	0.37	-0.03	0.03	-0.04	-0.03	-0.01	0.07	-0.02	-0.05	0.04	-0.03	-0.04	0.02	0.09
P2	0.04	0.35	0.23	0.22	-0.02	0.02	-0.02	-0.02	0.04	-0.01	0.05	0.01	-0.02	-0.02	0.11	0.03
P3	0.14	0.14	0.22	0.02	0.14	0.15	0.02	-0.01	0.06	0.02	0.01	0.05	0.01	0.00	0.01	0.01
P4	-0.02	0.22	0.04	0.34	-0.01	0.23	-0.02	0.03	0.02	0.06	0.09	0.03	0.02	-0.02	0.02	-0.03
P5	0.02	-0.02	0.24	-0.02	0.36	0.03	0.23	-0.02	0.00	-0.04	-0.02	0.05	0.02	0.10	0.01	0.06
P6	-0.01	0.01	0.14	0.14	0.02	0.21	0.14	0.14	0.00	0.03	0.00	0.02	0.07	0.01	0.06	0.02
P7	-0.02	-0.02	0.02	-0.02	0.24	0.24	0.36	0.03	-0.02	0.03	-0.02	0.06	0.02	0.06	0.02	0.02
P8	-0.02	-0.03	-0.04	0.04	-0.04	0.41	0.06	0.62	-0.04	0.11	-0.04	-0.02	0.03	-0.06	0.03	-0.02
B1	0.01	0.01	0.01	0.00	0.00	0.00	0.00	0.00	0.92	0.01	0.01	0.01	0.00	0.00	0.01	0.01
B2	0.00	0.00	0.00	0.01	-0.01	0.01	0.00	0.01	0.01	0.95	0.01	0.00	0.01	0.00	0.01	-0.01
B3	-0.01	0.01	0.00	0.02	0.00	0.00	0.00	0.00	0.00	0.00	0.96	0.00	0.00	0.00	0.02	0.00
B4	0.00	-0.01	0.01	-0.01	0.01	0.01	0.02	0.00	0.00	0.00	0.00	0.96	-0.01	0.01	0.02	0.01
B5	0.00	0.00	0.00	0.00	0.00	0.02	0.02	0.01	0.00	0.01	0.00	-0.06	1.00	0.00	0.00	0.01
B6	0.00	0.01	0.01	0.01	0.02	0.01	0.02	0.01	0.00	0.00	0.00	0.02	0.01	0.88	0.01	0.00
B7	0.00	0.01	0.01	0.01	-0.01	0.01	0.00	0.00	0.01	0.01	0.01	0.01	-0.01	0.00	0.94	-0.01
B8	0.01	0.00	0.01	0.00	0.01	0.00	0.00	0.00	0.01	0.00	0.00	0.01	0.00	0.00	0.00	0.95

Figure 5. *Matrix used for rejection correction derived from QEs (**Left**) and using the blind approach (**Right**) for square filters. Panchromatic bands are separated to due to spectral pixel proximity.*

bands, each of the eight pixels in the SFA pattern is considered separately when correcting spectral bands, as QE fits show strong contributions of the nearby filters. Results of this first correction are provided in Figure 4 using the rejection matrix provided in Figure 5 (*Left*) for square filters. Despite an accurate QE fit, the correction does not provide a significant improvement when applied on original images; in particular, the quincunx pattern of the panchromatic bands is enhanced by this spectral correction (and despite subsequent denoising). No difference is observed for the square or the octagonal filter configuration.

Blind correction approach

To compensate the spectral band rejection, a second method was implemented. Knowing that no pixelated artifact should be visible on uniform areas, we used this caveat to compute a correction matrix A'. This is performed by isolating uniform areas in the data set and computing, through least-squares minimization, the best coefficients for each band. Similarly to the previous method, this correction can be computed at a single 4×4 pattern level, or considering the closest neighbors weighted by their distance. The new matrix for the central pattern is provided Figure 5 (*Right*).

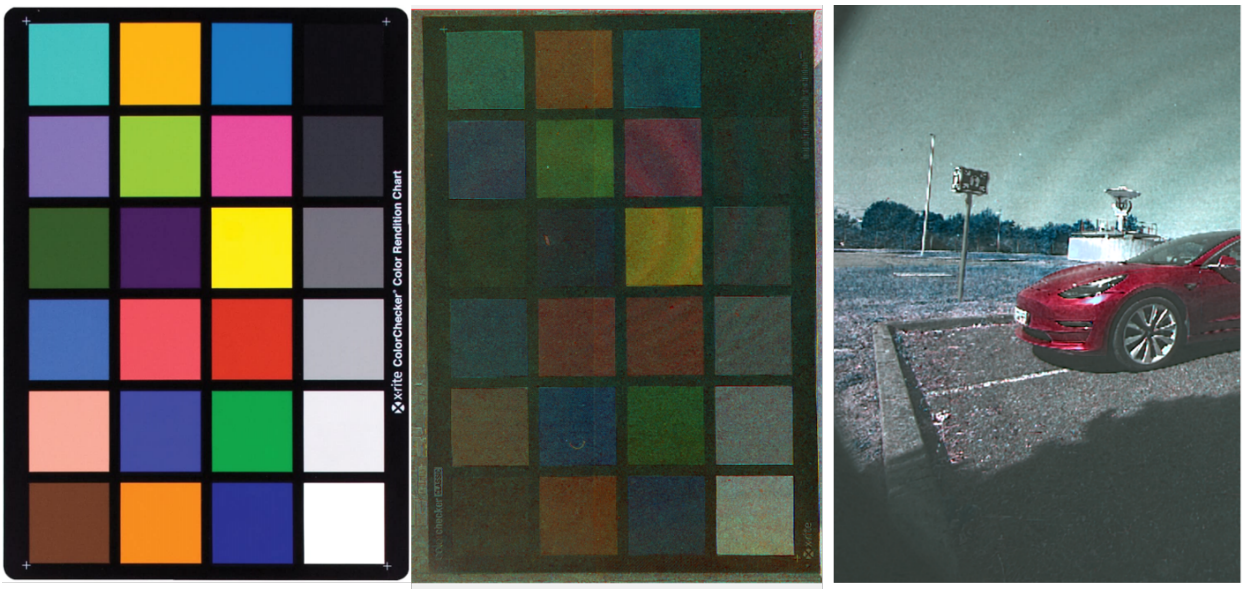

Figure 6. *(**Left**) ColorChecker target. (**Center**) Recovered color target after CCM correction on a SFA image (flatfield corrected, without IR cut-off filter). (**Right**) CCM applied to an image in the data set to recover the sRGB image, recovering the red hue of the car.*

This 'blind' approach provides a more robust and efficient correction than its previous counterpart.

When comparing the correction matrices, panchromatic bands have much lower coefficients than previously determined. This implies that a larger part of their signal is shared with nearby bands. The opposite trend appears in the spectral bands, which maintain a higher fraction of their original signal, while receiving data from neighboring panchromatic bands. Spectral contamination may thus be related to a combination of diffusion effects in the detector (whose bands are mostly in the NIR) and incident light scattering effects. We notice additionally that small negative contributions appear. This feature is not properly explained, but may be related to degeneracies in the least-squares fit for high-wavelength bands, particularly affected by shot noise. Equivalent trends are found in both square and octagonal filters, although correction coefficients are higher for the latter. This is expected, as octagonal filters overlap with panchromatic pixels, increasing spectral mixing by design. Further investigations of dedicated correction kernels for each band (convolutive correction) will be investigated in a forthcoming study.

Colorimetry and image visualization

The use of demosaicing on the SFA images provides an estimate of the spectral bands. A direct superposition of these bands to create RGB-like images can be performed for image quality purposes (Figure 2, 4), but does not provide realistic color details. In particular since blue bands are absent, the notion of color restitution (in the perceptional sense) is but a conceptual exercise [9]. The reconstruction of a reliable color image could however be particularly useful (see [12]) and would provide a comprehensive use of the cameras giving it a spatial, a spectral *and* a (limited) color dimension. In CFAs, the color correction is estimated by comparing the measured radiometry of the band i

$$B_i = \int_{VIS} R(\lambda) I(\lambda) QE_i(\lambda) d\lambda$$

where R is the reflectance, I the illuminant spectral power distribution (SPD) and QE_i the QE of RGB bands, to the expected standard color vision description, or Color Matching Functions (CMF), from ISO/CIE 11664 1931 standard:

$$\{X/Y/Z\} = \int_{VIS} R(\lambda) I(\lambda) \{\bar{x}(\lambda)/\bar{y}(\lambda)/\bar{z}(\lambda)\} d\lambda$$

where $\bar{x}, \bar{y}$ and $\bar{z}$ are the color matching functions (CMFs) of the human eye to RGB bands. Both can be shown in chromatic space with reduced coordinates (x,y), $x = X/(X+Y+Z)$ and $y = Y/(X+Y+Z)$ [10]. This allows to determine a color correction matrix $\mathscr{M}$ such that $(R,G,B) = \mathscr{M} \times (X,Y,Z)$.

To test color restitution in SFAs, a similar approach can be performed. In this case, we can express the same problem by $(B_i)_{i\in N} = \mathscr{M}' \times (X,Y,Z)$, with $\mathscr{M}'$ now a rectangular matrix of size $(N,3)$ where N is the number of spectral bands (9 here). This matrix was computed through a pseudo-inverse matrix using ground measurements at ISAE over a ColorChecker Classic X-rite target, with and without a IR cut-off filter in front of the SFA. A proper minimization was not performed to avoid introducing improper convergence results in the CCM [20]. The CCM computed without the IR filter for the nine bands $(P, B_{i\in\{1..8\}})$ is

$$\begin{pmatrix} -1.49 & -0.14 & 2.15 & 0.86 & -2.96 & 3.66 & 3.09 & -0.32 & -3.23 \\ -1.54 & -0.15 & 0.76 & 2.10 & -3.25 & 6.50 & 4.37 & -1.84 & -5.10 \\ 0.43 & -1.57 & -0.45 & 3.41 & -2.72 & 3.06 & 9.93 & -6.16 & -4.37 \end{pmatrix}$$

This matrix can be applied either to the color target image, or to any other image taken in the same conditions, to provide to the images to provide an sRGB color image of the observed scene. Results are shown in Figure 6. Surprisingly, we notice that despite the lack of blue information, blue hues can be observed. As the CCM is computed using multiple NIR and panchromatic information, we posit that these offer additional degrees of freedom in the minimization to recover blue hues. These should *not*

be considered as true blue hues, rather the missing colors below 550 nm are filled by combinations of the NIR information creating a "composite" blue. This conclusion can also be seen Figure 7, where blue hues are the least faithful. Recovered colors are not satisfactory using typical standards ($\geq 20\Delta E_{2000}$), and sRGB images also have a bluer hue than expected, likely related to the introduction of blue information from the NIR channels. Nonetheless, this crude approach provides some information (e.g. overall car color on Figure 6). The corrected images also show a strong noise, due to CCM coefficients in the NIR bands (particularly B6 and B7). New measurements of the color target (also using theoretical QEs) with a much higher signal-to-noise ratio will be conducted in the upcoming months to investigate possible improvements. These results show that these cameras could be interestingly leveraged to obtain basic color (in addition to spatial and spectral) information of nearby planetary bodies using a compact hardware. Further, should a more linear (radiance-based) approach be used [16], spectral information of the observed scene could be included to improve this correction. In this regard, this work should be considered as a first step for colorimetric studies of SFAs. A proper color correction must thus be considered jointly with the entire image restoration process.

Conclusion

The use of spectral filter array provides an elegant and efficient solution to space missions, in particular to planetary rovers, as it provides both imaging and spectral capabilities. These matrices also provide a compact view of the scene, which can be highly beneficial knowing the very few images that can be downlinked. The challenges of the data analysis are shifted towards the ground segment, as a proper demosaicing and spectral analysis require dedicated post-processing. In this paper, using a prototype SFA, we demonstrated a successful way to improve the image quality through the use of a non-local demosaicing. We also showed that a good knowledge of the SFA's properties can be used either to compensate for spectral rejections between bands (thus improving spectral resolution) but also to provide a coarse color information on the scene under observation.

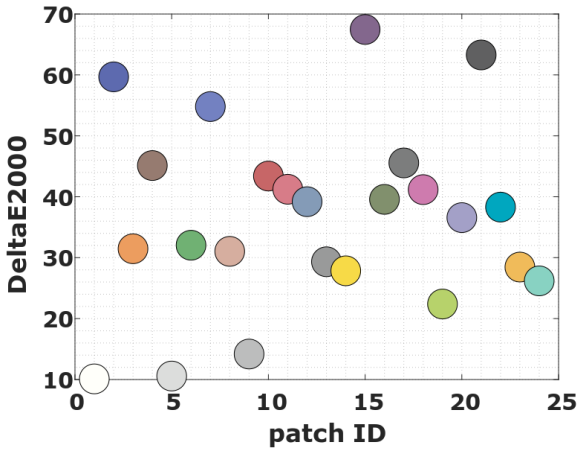

Figure 7. *Estimated ΔE_{2000} residuals after color correction, using the previous CCM. Results are not satisfactory and show that blue (or blue-related) hues have the worst accuracy.*

Similar SFA detectors are considered by CNES for future rover missions, in particular for the exploration of the lunar surface. This work highlights that entire image processing chain for such missions should always consider spectral, spatial and color issues jointly to achieve an optimal working point. Further developments of image quality principles for multi-spectral cameras are therefore critical, and shall be explored further in the upcoming years.

References

[1] P. Dillon, D. Lewis, and F. Kaspar, "Color imaging system using a single ccd area array," *IEEE Transactions on Electron Devices*, vol. 25, no. 2, pp. 102–107, 1978.

[2] T. Lule, S. Benthien, H. Keller, and al., "Sensitivity of cmos based imagers and scaling perspectives," *IEEE Transactions on Electron Devices*, vol. 47, no. 11, pp. 2110–2122, 2000.

[3] P.-J. Lapray, X. Wang, J.-B. Thomas, and P. Gouton, "Multispectral filter arrays: Recent advances and practical implementation," *Sensors*, vol. 14, pp. 21626–21659, Nov. 2014.

[4] S. Maurice, R. C. Wiens, P. Bernardi, and al., "The supercam instrument suite on the mars 2020 rover: Science objectives and mast-unit description," *Space Science Reviews*, vol. 217, p. 47, Apr 2021.

[5] S. Ulamec, P. Michel, M. Grott, and al., "A rover for the jaxa mmx mission to phobos," in *IAC 2019*, pp. IAC–19, International Astronautical Federation, October 2019.

[6] N. Longbotham, F. Pacifici, S. Malitz, and al., "Measuring the spatial and spectral performance of worldview-3," in *Fourier Transform Spectroscopy and Hyperspectral Imaging and Sounding of the Environment*, p. HW3B.2, Optica Publishing Group, 2015.

[7] M. Boutillier, K. Mathieu, S. Petit-Poupart, and al., "Pixelated multi-spectral filters assessment for space applications," in *International Conference on Space Optics — ICSO 2022*, International Society for Optics and Photonics, SPIE, 2022.

[8] D. Menon and G. Calvagno, "Color image demosaicking: An overview," *Signal Processing: Image Communication*, vol. 26, no. 8, pp. 518–533, 2011.

[9] A. Clouet, J. Vaillant, and D. Alleysson, "Physical noise propagation in color image construction: a geometrical interpretation," in *Color Imaging Conference 27*, (Paris, France), Oct. 2019.

[10] G. D. Finlayson, M. Mackiewicz, and A. Hurlbert, "Color correction using root-polynomial regression," *IEEE Transactions on Image Processing*, vol. 24, no. 5, pp. 1460–1470, 2015.

[11] E. Robert, M. Estribeau, R. Barbier, and al., "Impact of the training data in LLS optimizatio for faithful scene-specific color correction of RAW images," in *2021 Congress of The International Association of Color*, vol. 1, (Milan), pp. 287–292, 2021.

[12] J. N. Maki, D. Gruel, C. McKinney, and al., "The mars 2020 engineering cameras and microphone on the perseverance rover: A next-generation imaging system for mars exploration," *Space Science Reviews*, vol. 216, p. 137, Nov 2020.

[13] C. Sellier, D. Gambart, N. Perrot, and al., "Development and qualification of a miniaturised CMOS camera for space applications (3DCM734/3DCM739)," in *International Conference on Space Optics — ICSO 2018*, vol. 11180, pp. 1134 – 1140, International Society for Optics and Photonics, SPIE, 2019.

[14] S. Farsiu, M. Elad, and P. Milanfar, "Multiframe demosaicing and super-resolution of color images," *IEEE Transactions on Image Processing*, vol. 15, no. 1, pp. 141–159, 2006.

[15] R. Tan, K. Zhang, W. Zuo, and L. Zhang, "Color image demosaicking via deep residual learning," in *Proc. IEEE Int. Conf. Multimedia Expo (ICME)*, pp. 793–798, 2017.

[16] P. Amba, J. B. Thomas, and D. Alleysson, "N-lmmse demosaicing for spectral filter arrays," *Journal of Imaging Science and Technology*, vol. 61, no. 4, pp. 40407–1–40407–11, 2017.

[17] M. Lebrun, A. Buades, and J.-M. Morel, "Implementation of the "Non-Local Bayes" (NL-Bayes) Image Denoising Algorithm," *Image Processing On Line*, vol. 3, pp. 1–42, 2013.

[18] J. E. Adams and J. F. J. Hamilton, "Adaptive color plane interpolation in single sensor color electronic camera," 1996.

[19] M. A. Green, "Self-consistent optical parameters of intrinsic silicon at 300 k including temperature coefficients," *Solar Energy Materials and Solar Cells*, vol. 92, p. 1305–1310, 2008.

[20] R. S. Berns, "Image quality degradation caused by color transformations in multispectral imaging—a practical review," in *Archiving Conference*, vol. 17, pp. 60–67, Society for Imaging Science and Technology, 2020.

Acknowledgments

The authors would like to acknowledge SILIOS for their help and support for this study, as well as for providing the necessary hardware to conduct this analysis.

Author Biography

Dr. Edoardo Cucchetti has received his M.Sc. in engineering from the Ecole Polytechnique, Paris (2016) and his Ph.D. in space instrumentation from the Paul Sabatier University, Toulouse (2019). He is a full time engineer at the French Space Agency (CNES). His focus is on instrumentation, performance engineering and image quality, in particular the development of image quality techniques for future planetary rovers.